JACS
JOURNAL OF THE AMERICAN CHEMICAL SOCIETY
pubs.acs.org/JACS
Article

Broadband Achromatic Quarter-Waveplate Using 2D Hybrid Copper Halide Single Crystals

Yixuan Dou, Marie Solange Tumusange, Jianbo Jin, Xiaoming Wang, Erin R. Crater, Sunhao Liu, Liyan Zhu, Samir Zuberi, Gavin Harman, Conner Weaver, Balaji Ramanujam, Ambalanath Shan, Robert B. Moore, Nikolas J. Podraza, Yanfa Yan, and Lina Quan*

Cite This: J. Am. Chem. Soc. 2023, 145, 18007−18014

ABSTRACT: Achromatic quarter waveplates (A-QWPs), traditionally constructed from multiple birefringent crystals, can modulate light polarization and retardation across a broad range of wavelengths. This mechanism is inherently related to phase retardation controlled by the fast and slow axis of stacked multi-birefringent crystals. However, the conventional design of A-QWPs requires the incorporation of multiple birefringent crystals, which complicates the manufacturing process and raises costs. Here, we report the discovery of a broadband (540−1060 nm) A-QWP based on a two-dimensional (2D) layered hybrid copper halide (HCH) perovskite single crystal. The 2D copper chloride ($CuCl_6$) layers of the HCH crystal undergo Jahn−Teller distortion and subsequently trigger the in-plane optical birefringence. Its broad range of the wavelength response as an A-QWP is a consequence of the out-of-plane mosaicity formed among the stacked inorganic layers during the single-crystal self-assembly process in the solution phase. Given the versatility of 2D hybridhalide perovskites, the 2D HCH crystal offers a promising approach for designing cost-effective A-QWPs and the ability to integrate other optical devices.

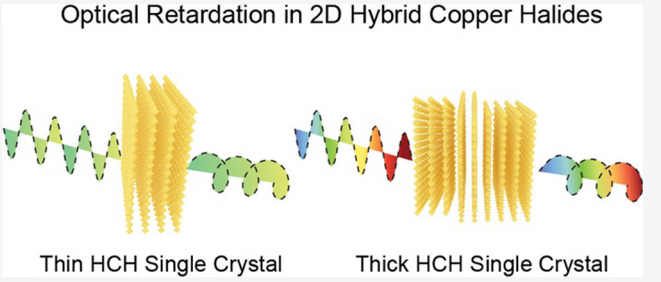

INTRODUCTION

Birefringence is a well-known phenomenon in which an anisotropic crystal exhibits different refractive indices depending on the polarization and propagation direction of the light that can split an incident light beam into a slow ray and a fast ray.[1] Birefringent crystals serve as the basis for constructing various types of waveplates, including half-waveplates (HWPs) and quarter waveplates (QWPs). The degree of phase retardation in waveplates is dependent on several factors including the incident beam wavelength, crystal birefringence value (Δn), and crystal thickness, which can be precisely controlled.[2] Waveplates made from a single-crystal component face limitations in achieving the desired phase retardation at a specific wavelength, since the amount of phase retardation is directly proportional to the wavelength. The incorporation of multiple birefringent crystals enables the waveplate to effectively operate over a wide range of wavelengths, providing broadband phase retardation, resulting in an Achromatic-QWP (A-QWP).[3−5] However, the traditional approach for fabricating A-QWPs involves a complex and high-cost multistep process with high commercial costs, which requires selecting and incorporating birefringent crystals with optimized thicknesses and birefringence values.

The recent emergence of 2D materials, such as transition metal dichalcogenides and halide perovskites, presents new opportunities for creating birefringent crystals.[6−12] The incorporation of organic components in 2D halide perovskites provides a high degree of tunability and programmability in both crystal structure and optical anisotropy.[13] Furthermore, single crystals of 2D halide perovskites can be synthesized in the solution phase, near room temperature, and at atmospheric pressure, and a large crystal flake can be obtained, which is favorable for fabricating optical waveplates. This facile wet-chemistry synthesis motivates the production of new-generation optical materials with reduced costs, high throughput manufacturing, and improved reproducibility.

Here, we report that the single crystalline 2D hybrid copper halide (HCH) perovskites show in-plane optical anisotropy due to the Jahn−Teller (JT) distortion in copper halide octahedral layers. This JT distortion leads to an in-plane birefringence factor of approximately 0.026 across a range from visible light to near-infrared light (NIR), based on the first-principles density functional theory (DFT) calculations. First, we demonstrate that the relatively thin (~34 μm) birefringent HCH crystal (PEA_2CuCl_4, PEA = phenylethylammonium) can

Received: May 31, 2023
Published: August 4, 2023

https://doi.org/10.1021/jacs.3c05705
J. Am. Chem. Soc. 2023, 145, 18007−18014

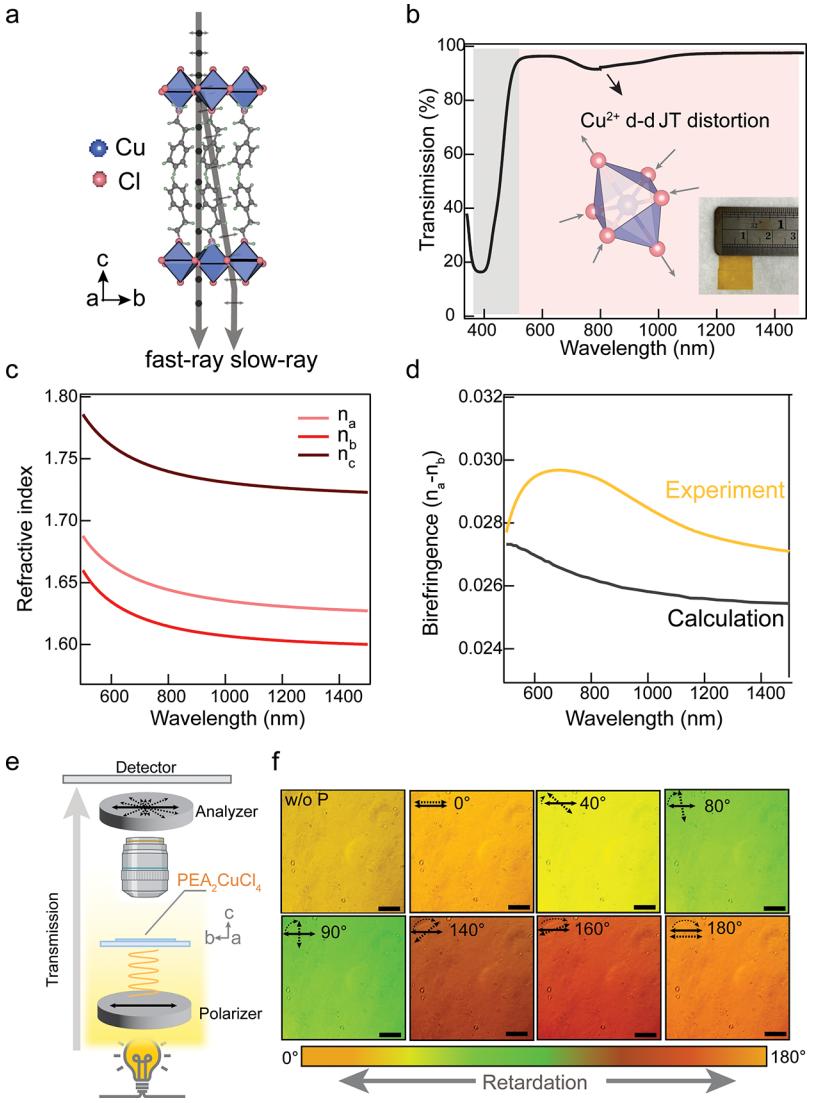

Figure 1. (a) Crystal structure of HCH crystals with a schematic illustration of birefringence with gray arrows. (b) Transmission spectrum of the HCH crystal from ultraviolet (UV) to NIR wavelengths with the inset showing the photograph of an HCH crystal. (c) In-plane refractive indexes from spectroscopic ellipsometry. (d) Birefringence $\Delta n(n_a - n_b)$ factor from spectroscopic ellipsometry measurement and theoretical calculation. (e) Schematic diagram of the configuration of a polarized optical microscopy setup. (f) Polarized optical microscope image of the HCH crystal (164 μm in thickness) as a function of different analyzer angles; the scale bar in the image is 5 μm.

be utilized as a QWP, which converts linearly polarized light to circularly polarized light or vice versa at λ = 920 nm. Subsequently, we show that the thick (~164 μm) HCH single crystal can function as an A-QWP that effectively modulates the light polarization across a broad range of wavelengths from visible light to NIR (λ = 540−650, 805−820, and 1000−1060 nm) without necessitating intricate designs. In addition, HCH crystals possess exceptional air stability and forbidden optically induced luminescence properties, thereby minimizing artifacts that typically arise from band gap photoluminescence (PL) emission that is frequently encountered in the lead (Pb)-based 2D halide perovskites.[14,15] By employing a combination of grazing-incidence wide-angle X-ray scattering (GI-WAXS) and single-crystal X-ray diffraction (SCXRD) analysis, we have found that the A-QWP property of the HCH crystal is attributed to the out-of-plane mosaicity of the stacked inorganic layers. The weak interlayer van der Waals forces between the 2D layered HCH crystal encourages the naturally forming interlayer dislocations and twists. The out-of-plane mosaicity in the inorganic layers of an individual thick HCH crystal makes it behave similarly to an amalgamation of numerous birefringent crystals with different fast-axis orientations for each of them. As a result, an individual HCH crystal can directly be utilized as an A-QWP, obviating the requirement for multiple crystals. Our findings indicate that these 2D HCH crystals have the potential to enable the development of cost-effective, single-component A-QWPs for multispectral photonic components and optical device applications.

RESULTS AND DISCUSSION

A high-quality, centimeter-sized flake of HCH (PEA_2CuCl_4; PEA = phenylethylammonium) single crystal was prepared using a standard slow-cooling crystallization method from an aqueous solution. The crystal image is shown in the inset image of Figure 1b. An orthorhombic unit cell of PEA_2CuCl_4 was determined from SCXRD, which showed a layered structure composed of inorganic octahedra and organic cation

https://doi.org/10.1021/jacs.3c05705
J. Am. Chem. Soc. 2023, 145, 18007−18014

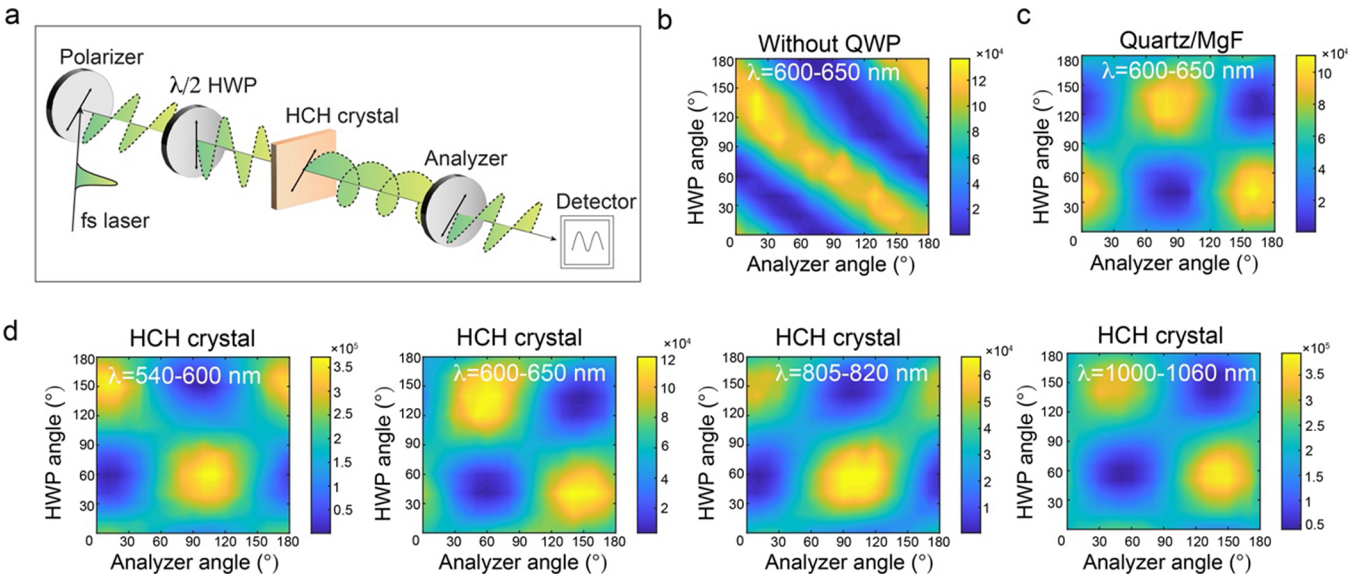

Figure 2. (a) Schematic diagram of the laser polarization modulation measurement setup. (b) Transmitted laser intensity changes with the laser modulation setup without a sample at the wavelength of 600−650 nm. (c) Transmitted laser intensity change with commercial quartz/MgF_2 QWP at the wavelength of 600−650 nm; (d) transmitted laser intensity changes with the HCH crystal in between HWP and an analyzer (at the wavelength of 540−600, 600−650, 805−820, 1000−1060 nm from left to right).

layers, as illustrated in Figure 1a.[16] The $3d^9$ electronic configuration of Cu^{2+} gives rise to significant JT distortion.[17−19] As shown in Figure 1b, the weak absorption feature induced by the d−d transition of the copper chloride octahedra can be observed in the NIR (800−1000 nm) region.[20,21] The JT distortion plays a crucial role in reducing the energy and results in elongated copper halide octahedra, enabling anisotropic lattice distortions in both out-of-plane and in-plane directions.[19] The presence of in-plane structural anisotropy is essential for generating in-plane optical birefringence which is still challenging for common 2D hybrid halide perovskites. To quantitatively study the optical birefringence, we performed spectroscopic ellipsometry to confirm the refractive indices at both in-plane and out-of-plane directions, as depicted in Figure 1c,d. Notably, the HCH crystal shows an in-plane birefringence factor with the $\Delta n(n_a - n_b)$ value about 0.028−0.029 from visible to the NIR region based on the ellipsometry measurement. Then, we further confirmed the in-plane birefringence of the HCH crystal via the first-principles calculations (Figures 1d and S1). The birefringence value from calculation agrees well with the experimental result, which is comparable to the birefringence factor from standard QWP materials (Table S1).

Then, cross-polarized optical microscopy (CPOM) was employed to visualize the optical anisotropy and further identify birefringence by monitoring the crystal interference color. Figure 1e illustrates the CPOM setup, where a polarizer and an analyzer were positioned before and after the sample in the perpendicular direction, respectively. The birefringent crystal split the incident beam into fast and slow rays that are vectorially recombined after passing through the analyzer. The phase retardation between two rays results in destructive interference for lights at certain wavelengths, which leads to interference colors in the CPOM. Therefore, the interference color is controlled by the phase retardation, which is determined by the crystal thickness and birefringence, as described in the equation: R (radian) = $2\pi \times \Delta n \times T/\lambda$ (R is phase retardation, T is the thickness, λ is the wavelength).[1] The HCH crystal with uniform thickness and a smooth surface (Figure S2) showed a uniform bright green color under CPOM (Figure 1f). By rotating the analyzer from 0° to 90°, the crystal color changed substantially due to the retardance change, leading to the interference color change from yellow to green to red. To quantify the interference color change, the RGB values of the CPOM microscopy color at different analyzer angles were extracted (Table S2). As the angle difference between the polarizer and analyzer increased from 0° to 180°, both R and G values changed periodically (Figure S3), which further confirmed the in-plane birefringence of the HCH crystal.

To further prove that the origin of the in-plane birefringence of 2D HCH crystal is due to JT effects in copper halide layers, we studied the in-plane birefringence of hybrid metal halide crystals via chemical structure engineering with various organic ligands, metal cations, and halide anions. On the one hand, when the organic ligands were varied while keeping the same copper halide building blocks, the HCH crystal retained the desirable in-plane birefringence, as shown in the CPOM images (Figure S4). This indicated that the in-plane anisotropy of HCH crystal is not significantly affected by the organic spacer layer in the case of copper chloride-based system. On the other hand, we engineered both metal cation and halide ions to further study the effect of JT distortion. After replacing the copper Cu^{2+} with lead Pb^{2+} cations in the inorganic layer, while maintaining the same PEA organic spacer, we did not observe evidence of in-plane birefringence from the PEA_2PbBr_4 crystal with a thickness of approximately 88 μm (Figure S5). Since it is known that the lead halide system does not retain JT distortion,[20] the nonexistence of in-plane birefringence further indicated the crucial role of JT distortion to in-plane birefringence in HCH crystals. We then alloyed 50% of Br into the pure chloride-based HCH crystal as $PEA_2CuCl_2Br_2$, and the Br-alloyed HCH again showed the in-plane birefringence (Figure S6). However, the interference color showed limited changes when the analyzer angle was rotated, due to a reduced in-plane birefringence and enhanced

https://doi.org/10.1021/jacs.3c05705
J. Am. Chem. Soc. 2023, 145, 18007−18014

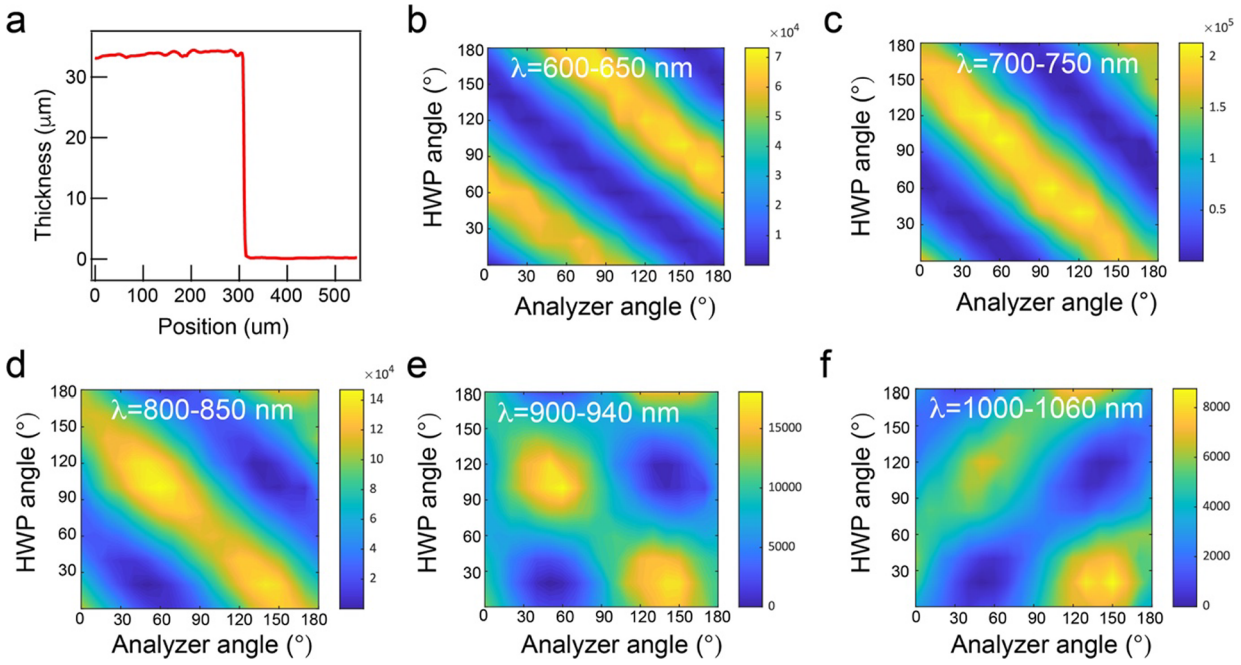

Figure 3. (a) Thickness diagram of the HCH crystal with a thickness of 34 μm. (b–f) Transmitted laser intensity changes from the HCH crystal as a wave plate with a thickness of 34 μm, measured from the wavelength of 600–650, 700–750, 800–850, 900–950, and 1000–1060 nm.

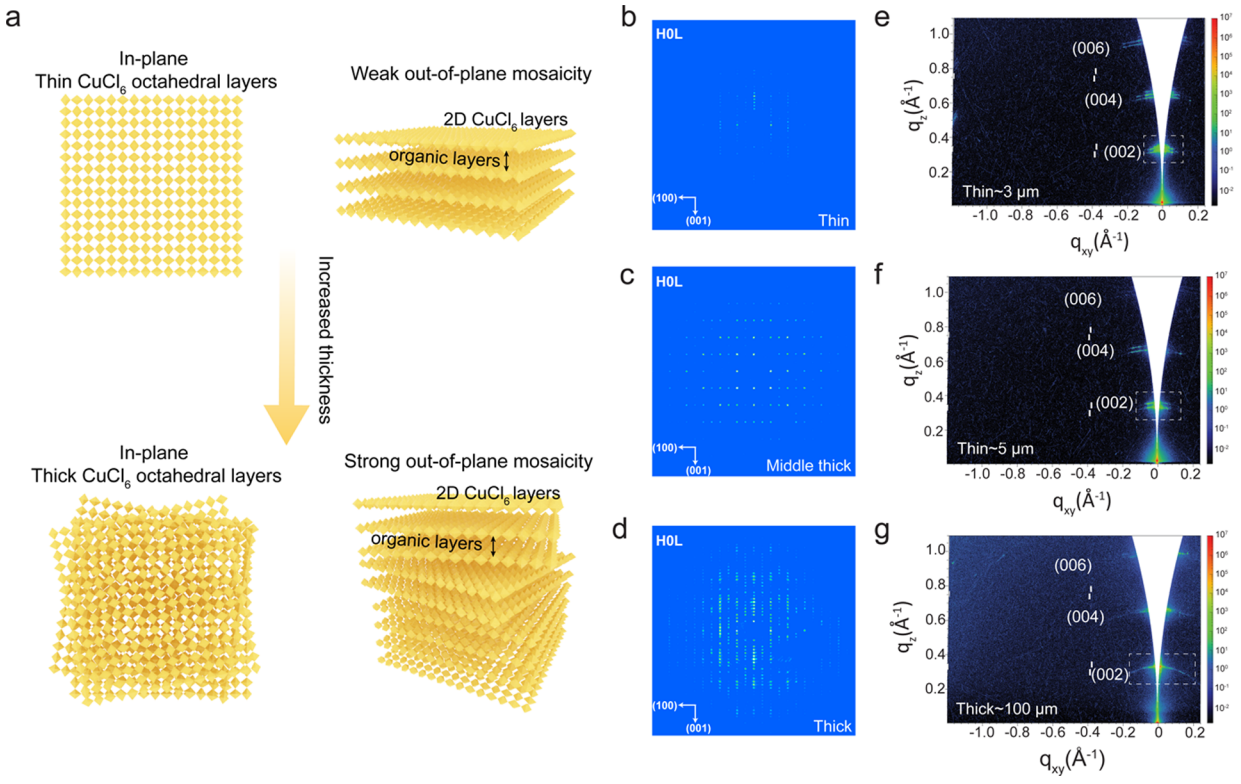

Figure 4. (a) Schematic diagram that shows the formation of out-of-plane mosaicity between thin and thick single crystals. SCXRD unwraped images generated from the (100) and (001) crystallographic axes of (b) thin HCH crystal, (c) middle-thick HCH crystal, and (d) thick HCH crystal. GI-WAXS measurements for the HCH crystals with varied thicknesses (e), 3 μm, (f) 5 μm, and (g) 164 μm.

absorption of the crystal in the visible range. We thought the weakening of in-plane birefringence could be correlated with changes in the degree of JT distortion. Therefore, the crystal structure engineering provides compelling evidence that the in-plane birefringence is mainly impacted by JT distortion in copper halide octahedra layers.

The in-plane birefringence is crucial for their applications in fabricating waveplates, indicating that the HCH crystal is a promising candidate for waveplate materials. To evaluate the potential of HCH crystals as waveplates, we conducted laser modulation measurements.[22] The laser modulation measurement setup is depicted in Figure 2a, and a detailed explanation

https://doi.org/10.1021/jacs.3c05705
J. Am. Chem. Soc. 2023, 145, 18007–18014

of the setup is in the Methods section. We used a wavelength-tunable femtosecond laser as an incident light source and linearly polarized laser light was directed perpendicular to the in-plane direction of a 2D HCH single crystal. As shown in Figure 2b,c, when the crystal was absent from the beam path, the laser was fully linearly polarized and showed parallel stripes in the 2D colormap graph. When adding a commercial QWP (made from quartz andMgF_2) to the beam path, the colormap showed clear circles indicative of waveplate behavior.

Initially, we measured the HCH crystal with a thickness of 34 μm, and the clear circles are observed in the color map from 900−940 nm, similar to the commercially available multiorder QWP as illustrated in Figures 3 and S7 (as demonstrated by the original laser spectrum in Figure S8), indicating that the HCH crystal can function as single wavelength QWP. Subsequently, a thicker HCH crystal with a thickness of 164 μm was measured (Figure S9), and the thicker HCH crystal showed unexpected A-QWP properties over a broad range of wavelengths from visible to NIR, including λ = 540−650, 800−820, and 1000−1060 nm (Figure 2d). We then analyzed another HCH crystal with a thickness of 237 μm (Figure S10), which displayed a slightly distinct but again a broad wavelength response at λ = 550−650, 700−750, and 800−850 nm. These results indicate that the wavelength response range of A-QWP HCH crystal is dependent on crystal thickness. Furthermore, in addition to testing the laser modulation properties with pulsed lasers, we also conducted experiments using a continuous wavelength laser, which demonstrated similar effects (Figure S11). In addition, we utilized a different laser modulation setup to further confirm the QWP properties (Figure S12). A commercialized QWP was placed after the HCH crystal, and the laser became circularly polarized light after passing through HCH crystal, then after passing through the commercialized QWP, the laser became linearly polarized light again. This measurement provides further evidence of the QWP property of the HCH crystal. The manifestation of such an A-QWP property within a monostructured single crystal underscores the uniqueness and potential of HCH crystals for future photonic applications.

Typically, conventional A-QWPs are fabricated by combining multiple birefringent crystals. This is often interpreted by calculating the combined retardation of N birefringent crystals with a thickness of d_i and a birefringence value of n_i as follows: $R_{\text{combined}} = \sum_{i=1}^{N} \frac{n_i}{\lambda} d_i$.[3−5] In contrast, our A-QWP is based on an individual HCH single crystal without any heterostructure or multicomponent design. The HCH's broadband retardation is possibly due to dislocation and distortion between the stacked inorganic layers, so-called out-of-plane mosaicity.[23,24] The HCH crystals used in the laser modulation measurement had a thickness of approximately 164 μm (Figure S9), and the distance between two copper chloride inorganic layers is estimated to be around 1.9 nm based on the lattice parameter determined from SCXRD. Out-of-plane dislocations and twists are anticipated to appear among the hundreds of copper chloride inorganic layers within the thick bulk HCH crystal with weak interlayer van der Waals interactions, leading to disordered stacked inorganic layers, as illustrated in Figure 4a. As a result, we did not observe the A-QWP property in thinner HCH crystals (34 μm) due to the relatively ordered stacking of the crystals in the out-of-plane direction. Thus, the thick HCH single-crystal possesses disordered stacking of inorganic layers, which can be seen as a combination of multiple birefringent HCH thin layers. This combination is responsible for the broadband retardation observed in the material.

To substantiate the presence of out-of-plane mosaicity, we performed SCXRD measurements on three bulk HCH crystals of different thicknesses: thin, middle-thick, and thick samples (crystal images are shown in Figure S13a−c). The utilization of unwarped images, constructed from the raw diffraction frames, facilitated the examination of diffraction features arising from misalignment along the c-axis.[25] Notably, our findings demonstrate that thicker crystals exhibit not only much stronger diffractions but also exhibit significant smearing effects along the ⟨010⟩ axis in the unwarped images generated from the (100) and (001) crystallographic axes (Figure 4b−d). Interestingly, this phenomenon is also observable in the (0KL) unwarped image, albeit absent in the (HK0) counterpart (see Figures 4b−d and S13d−f). This observation provides compelling evidence that increased crystal thickness correlates with a higher degree of misalignment within the inorganic layers. These measurements provide direct evidence for the existence of out-of-plane mosaicity in the thick HCH crystals.

To further investigate the interlayer packing of the HCH crystal with different thicknesses, we performed GI-WAXS experiments on crystals with thicknesses ranging from 3 μm to 164 μm (Figure S14) and monitored the diffraction peak of the (0 0 2) plane and the (0 0 4) plane. The diffraction peaks of the thinnest HCH crystal with a thickness of 3 μm (Figure 4e) are more elaborate, sharper, and showed less out-of-plane order than the thickest crystal (Figure 4f,g), which showed significant streaking of the (0 0 2) reflection along q_{xy}. A broader range of GI-WAXS diffraction peaks with varied crystal thicknesses is shown in Figure S15. This provides direct evidence of the less ordered layer stacking arrangement of the thicker HCH crystal,[26,27] indicating that broadband retardation is attributed to the out-of-plane mosaicity. It is known that the A-QWPs can be fabricated with the combination of two or more different birefringent crystals, and the broad wavelength laser modulation range could be controlled by the angle between crystal fast axes.[3,4,28] Thus, the HCH A-QWPs wavelength range can be affected by the twisted angle between copper halide octahedra ($CuCl_6^{4-}$) layers along the c-axis. Therefore, multiple copper chloride inorganic layers with different twisted angles can lead to a broader achromatic wavelength range.

CONCLUSIONS

The high-quality large-area anisotropic 2D HCH layered crystal exhibited a desirable birefringence with an in-plane Δn about 0.026 from visible to NIR wavelengths. The anisotropy is proven to originate from the distortion of copper halide octahedra layers with JT distortion. The birefringent HCH crystal flake is able to function as a QWP that can modulate linearly polarized light to circularly polarized light or vice versa. In addition, the thick HCH crystal QWP covers a broad wavelength range from visible to NIR, indicating that HCH crystals can be used as A-QWP. Based on the GI-WAXS measurement and SCXRD data analysis from the HCHs with different thicknesses, the disordered stacked inorganic layers are responsible for the A-QWP property in a thick HCH single crystal. This work indicates that the 2D HCH perovskite is a promising candidate for fabricating economical A-QWPs and other optical devices.

https://doi.org/10.1021/jacs.3c05705
J. Am. Chem. Soc. 2023, 145, 18007−18014

EXPERIMENTAL SECTION

Crystal Synthesis. PEA_2CuCl_4: phenethylammonium chloride (PEACl) (473.9 mg) and 256.5 mg copper(II) chloride dihydrate were dissolved with 9 mL of methanol under 75 °C in an oil bath. Upon slow cooling down of the solution at 4 °C/h to 25 °C, a yellow PEA_2CuCl_4 crystal flake is obtained. The crystal is then washed with chloroform three times. $PEA_2CuCl_2Br_2$: using the same methods as PEA_2CuCl_4, the $PEA_2CuCl_2Br_2$ crystal is prepared by replacing 473.9 mg of PEACl with 404.18 mg of phenethylammonium bromide (PEABr).

Thin-Layer PEA_2CuCl_4 Crystal Preparation with the Space-Confinement Method. PEA_2CuCl_4 crystal solutions were prepared by directly dissolving washed crystals. The solution concentration is 200 mg/mL dissolving with dimethyl sulfoxide/γ-butyrolactone mixed solvent (7:3 volume ratio). Glass slides were cleaned for 15 min in an ultrasonic cleaner with water, 2-propanol, and then acetone, respectively. Petri dishes, glass slides, spacers (microscope slide covers), and PEA_2CuCl_4 crystal solutions were preheated on a hotplate for 10 min at 70 °C. Spacers were placed on both edges of the glass slide, and 10 μL crystal solution (preheated for 10 mins) is dropped in the middle of the glass slide. Then, another preheated glass slide is placed on the top. Another small Petri dish is placed on top of the glass slide(s) filled with 5 mL of chloroform. The Petri dish (containing the glass and small Petri dish) is closed and wrapped in foil for about 3 days to afford the thin crystal on the glass.

Characterizations. *UV−Vis−NIR Absorption.* The measurement is performed by a Hitachi U4100 from UV−Vis−NIR spectroscopy from Hitachi High Technologies.

Grazing-Incidence Wide-Angle X-Ray Scattering (GI-WAXS). The experiments were performed on a Xenocs Xeuss 3.0 SAXS/WAXS equipped with a GeniX 3D Cu HFVLF microfocus X-ray source utilizing Cu Kα radiation (λ = 0.154 nm). The sample-to-detector distance is 370 mm and calibrated using a silver behenate standard, and the incident angle was 0.2°. Two-dimensional scattering patterns were obtained using a Dectris EIGER 4 M detector and processed using the XSACT software package.

Single-Crystal XRD. Crystals with different thicknesses were cut into an irregular shape and centered on the goniometer of a Rigaku Oxford Diffraction Synergy-S diffractometer equipped with a HyPix6000HE detector and operating with Mo Kα radiation. CrysAlisPro[29] was used for data collection and data processing, including a multiscan absorption correction applied using the SCALE3 ABSPACK scaling algorithm. Using Olex2,[30] the structures were solved with the SHELXT[31] structure solution program using Intrinsic Phasing and refined with the SHELXL[32] refinement package using Least Squares minimization. Unwraped images built on integrative layers were also generated with the "Unwrap" functions in the CrysAlisPro software. The unwrap images were integrated with 7 units from −0.3 to 0.3.

Broadband Spectroscopic Ellipsometry Measurement. The measurement is performed using a single rotating compensator multichannel ellipsometer (M-2000XI, J.A. Woollam Co., Inc., Lincoln, NE, USA) on an anisotropic (001)-oriented HCH thin-layer single crystal on glass supporting substrate.[33,34] The light source wavelength range is 245−1598 nm. Generalized ellipsometric spectra are collected at angles of incidence of 45°, 55°, and 65° as a function of azimuthal rotations. Optical responses in the form of complex dielectric function ($\varepsilon = \varepsilon_1 + i\varepsilon_2 = N^2 = (n + ik)^2$) spectra for electric field oscillating parallel to the *a*-, *b*-, and *c*-crystallographic axes directions are modeled using a parametric model consisting of Sellmeier expressions,[35,36] a constant additive term to ε_1 denoted as ε_∞ and Tauc−Lorentz[37] or Gaussian oscillators.[38,39] The fit between experiment and model generated data is quantified with a mean square error (MSE) of 3.1×10^{-2}.

First-Principles DFT Calculations. The simulation was performed using the Vienna Ab Initio Simulation Package (VASP) code[40,41] with projector augmented-wave potentials.[42] An energy cut-off value of 400 eV is adopted to expand the wavefunctions and the Gamma-centered $2 \times 2 \times 1$ *k* mesh is considered when sampling the Brillouin zone. We used the experimental lattice parameters and relaxed the atomic coordinates using the Perdew−Burke−Ernzerhof[43] functional with a force tolerance of 0.01 eV/Å. The DFT+*U* scheme[44] with an effective *U* value of 7.28 eV for Cu was employed.

Laser Modulation Measurement. The laser modulation measurement setup is shown in Figure 2a. The laser is generated from the Astrella-F-1K one-box femtosecond amplifier of Coherent company with an optical parametric amplifier system. The polarizer, half waveplate, and QWP were purchased from Thorlabs, and the thin film polarizer works as an analyzer is purchased from Newport. The HRS-300 spectrometer with a PyLoN camera system from Princeton Instruments is used to detect the transmitted laser intensity. At first, the femtosecond pulsed laser passes through a linear polarizer, followed by a half waveplate that can tune the polarization direction. Then, the highly polarized light with tunable direction will pass through the PEA_2CuCl_4 crystal. If the PEA_2CuCl_4 crystal can function as a QWP, the light can be modulated to be circularly or elliptically polarized light when the angle difference between the laser fast axes and crystal fast axes is 45° or between 45° and 0°. Here, the half waveplate has rotated a total of 90°, which means the laser fast axes angle changed 180°. As the laser fast axes angle changes, the transmitted light will change from linear to elliptical and circularly polarized light if the PEA_2CuCl_4 crystal can function as a QWP, followed by an analyzer to detect the laser polarization direction. The transmitted light intensity is monitored when rotating the analyzer. When rotating the analyzer, the circularly polarized light intensity will show negligible change, the elliptical light intensity will show small change, and the linearly polarized laser will show tremendous change. A two-dimensional color map is obtained by recording the transmitted laser intensity upon half waveplate and the analyzer angle change. As shown in Figure 2b,c, the laser is fully linearly polarized without the crystal on the beam path, which exhibits parallel stripes in the 2D colormap graph. While with a commercial A-QWP in the beam path, the colormap shows clear circles.

ASSOCIATED CONTENT

Supporting Information

The Supporting Information is available free of charge at https://pubs.acs.org/doi/10.1021/jacs.3c05705.

In-plane refractive indexes from DFT calculations; AFM image of HCH crystal; exported red and green value from the polarized optical microscope image with HCH crystal; CPOM of A_2BX_4 crystals with different organic cations, halide, and metals; laser modulation measurement of 34 μm HCH crystal at an additional wavelength range; original laser spectra for laser modulation measurement; thickness measurement of HCH crystals; laser modulation measurement of 237 μm HCH crystal with fs laser and CW laser; laser modulation measurement with additional QWP of HCH crystal; SCXRD unwraped images and crystal images of HCH crystals with different thicknesses; and GI-WAXS with broader angle range of HCH crystals with different thicknesses (PDF)

AUTHOR INFORMATION

Corresponding Author

Lina Quan − *Department of Chemistry and Department of Materials and Science Engineering, Virginia Tech, Blacksburg, Virginia 24061, United States;* orcid.org/0000-0001-9301-3764; Email: linaquan@vt.edu

Authors

Yixuan Dou − *Department of Chemistry, Virginia Tech, Blacksburg, Virginia 24061, United States*

Marie Solange Tumusange − *Department of Physics and Astronomy and Wright Center for Photovoltaics Innovation and Commercialization, The University of Toledo, Toledo, Ohio 43606, United States*
Jianbo Jin − *Department of Chemistry, University of California, Berkeley, California 94720, United States;* orcid.org/0000-0002-9054-7960
Xiaoming Wang − *Department of Physics and Astronomy and Wright Center for Photovoltaics Innovation and Commercialization, The University of Toledo, Toledo, Ohio 43606, United States;* orcid.org/0000-0002-5438-1334
Erin R. Crater − *Department of Chemistry and Macromolecules Innovation Institute, Virginia Tech, Blacksburg, Virginia 24061, United States*
Sunhao Liu − *Department of Chemistry, Virginia Tech, Blacksburg, Virginia 24061, United States*
Liyan Zhu − *The Bradley Department of Electrical and Computer Engineering, Virginia Tech, Blacksburg, Virginia 24061, United States;* orcid.org/0000-0002-5415-676X
Samir Zuberi − *College of Science in the Academy of Integrated Science, Virginia Tech, Blacksburg, Virginia 24061, United States*
Gavin Harman − *Department of Chemical Engineering, Virginia Tech, Blacksburg, Virginia 24061, United States;* orcid.org/0009-0001-6078-7699
Conner Weaver − *The Bradley Department of Electrical and Computer Engineering, Virginia Tech, Blacksburg, Virginia 24061, United States*
Balaji Ramanujam − *Department of Physics and Astronomy and Wright Center for Photovoltaics Innovation and Commercialization, The University of Toledo, Toledo, Ohio 43606, United States*
Ambalanath Shan − *Department of Physics and Astronomy and Wright Center for Photovoltaics Innovation and Commercialization, The University of Toledo, Toledo, Ohio 43606, United States*
Robert B. Moore − *Department of Chemistry and Macromolecules Innovation Institute, Virginia Tech, Blacksburg, Virginia 24061, United States;* orcid.org/0000-0001-9057-7695
Nikolas J. Podraza − *Department of Physics and Astronomy and Wright Center for Photovoltaics Innovation and Commercialization, The University of Toledo, Toledo, Ohio 43606, United States*
Yanfa Yan − *Department of Physics and Astronomy and Wright Center for Photovoltaics Innovation and Commercialization, The University of Toledo, Toledo, Ohio 43606, United States;* orcid.org/0000-0003-3977-5789

Complete contact information is available at: https://pubs.acs.org/10.1021/jacs.3c05705

Notes

The authors declare no competing financial interest.

■ ACKNOWLEDGMENTS

This work was supported by Virginia Tech's Materials Characterization Facility under the Institute for Critical Technology and Applied Science, the Macromolecules Innovation Institute, and the Office of the Vice President for Research and Innovation. The purchase of the Xenocs Xeuss 3.0 SAXS/WAXS instrument used to obtain results included in this publication was supported by the National Science Foundation under the award DMR MRI 2018258. The first-principles calculations were performed using the resources of the National Energy Research Scientific Computing Center (NERSC), a US Department of Energy Office of Science User Facility located at Lawrence Berkeley National Laboratory, operated under contract DE-AC02-05CH11231 using NERSC award BES-ERCAP0017591. We thank the support of the National Science Foundation under CHE-1726077 for crystallography experiments. J Jin acknowledges his fellowship support from Suzhou Industrial Park.

■ REFERENCES

(1) Pedrotti, F. L.; Pedrotti, L. M.; Pedrotti, L. S. *Introduction to optics*; Cambridge University Press, 2019.
(2) Holbourn, A. Angular momentum of circularly polarised light. *Nature* **1936**, *137*, 31−31.
(3) McIntyre, C. M.; Harris, S. Achromatic wave plates for the visible spectrum. *J. Opt. Soc. Am.* **1968**, *58*, 1575−1580.
(4) Beckers, J. Achromatic linear retarders. *Appl. Opt.* **1971**, *10*, 973−975.
(5) Boulbry, B.; Bousquet, B.; Le Jeune, B.; Guern, Y.; Lotrian, J. Polarization errors associated with zero-order chromatic quarter-wave plates in the whole visible spectral range. *Opt. Express* **2001**, *9*, 225−235.
(6) Huang, W.; Zhang, X.; Li, Y.; Zhou, Y.; Chen, X.; Li, X.; et al. A Hybrid Halide Perovskite Birefringent Crystal. *Angew. Chem., Int. Ed. Engl.* **2022**, *61*, No. e202202746.
(7) Wang, J.; Ma, Y.; Wang, Z.; Liu, X.; Han, S.; Liu, Y.; et al. Unusual ferroelectric-dependent birefringence in 2D trilayered perovskite-type ferroelectric exploited by dimensional tailoring. *Matter* **2022**, *5*, 194−205.
(8) Ermolaev, G.; Grudinin, D.; Stebunov, Y.; Voronin, K. V.; Kravets, V.; Duan, J.; et al. Giant optical anisotropy in transition metal dichalcogenides for next-generation photonics. *Nat. Commun.* **2021**, *12*, 854.
(9) Munkhbat, B.; Wróbel, P.; Antosiewicz, T. J.; Shegai, T. O. Optical Constants of Several Multilayer Transition Metal Dichalcogenides Measured by Spectroscopic Ellipsometry in the 300−1700 nm Range: High Index, Anisotropy, and Hyperbolicity. *ACS Photonics* **2022**, *9*, 2398−2407.
(10) Hu, D.; Chen, K.; Chen, X.; Guo, X.; Liu, M.; Dai, Q. Tunable Modal Birefringence in a Low-Loss Van Der Waals Waveguide. *Adv. Mater.* **2019**, *31*, No. 1807788.
(11) Xu, H.; et al. Magnetically tunable and stable deep-ultraviolet birefringent optics using two-dimensional hexagonal boron nitride. *Nat. Nanotechnol.* **2022**, *17*, 1091−1096.
(12) Yang, H.; et al. Optical Waveplates Based on Birefringence of Anisotropic Two-Dimensional Layered Materials. *ACS Photonics* **2017**, *4*, 3023−3030.
(13) Saparov, B.; Mitzi, D. B. Organic−Inorganic Perovskites: Structural Versatility for Functional Materials Design. *Chem. Rev.* **2016**, *116*, 4558−4596.
(14) Valiente, R.; Rodriguez, F. Comment on "Copper-Substituted Lead Perovskite Materials Constructed with Different Halides for Working $(CH_3NH_3)_2CuX_4$-Based Perovskite Solar Cells from Experimental and Theoretical View". *ACS Appl. Mater. Interfaces* **2020**, *12*, 37807−37810.
(15) Yuan, M.; et al. Perovskite energy funnels for efficient light-emitting diodes. *Nat. Nanotechnol.* **2016**, *11*, 872−877.
(16) Polyakov, A. O.; et al. Coexisting Ferromagnetic and Ferroelectric Order in a $CuCl_4$-based Organic−Inorganic Hybrid. *Chem. Mater.* **2012**, *24*, 133−139.
(17) Asensio, Y.; Marras, S.; Spirito, D.; Gobbi, M.; Ipatov, M.; Casanova, F.; Mateo-Alonso, A.; Hueso, L. E.; Martín-García, B. Magnetic Properties of Layered Hybrid Organic-Inorganic Metal-Halide Perovskites: Transition Metal, Organic Cation and Perovskite Phase Effects. *Adv. Funct. Mater.* **2022**, *32*, No. 2207988.

(18) Kim, W. J.; Smeaton, M. A.; Jia, C.; Goodge, B. H.; Cho, B.-G.; Lee, K.; Osada, M.; Jost, D.; Ievlev, A. V.; Moritz, B.; Kourkoutis, L. F.; Devereaux, T. P.; Hwang, H. Y. Geometric frustration of Jahn−Teller order in the infinite-layer lattice. *Nature* **2023**, *615*, 237−243.
(19) Wang, S.; Khan, A. A.; Teale, S.; Xu, J.; Parmar, D. H.; Zhao, R.; Grater, L.; Serles, P.; Zou, Y.; Filleter, T.; Seferos, D. S.; Ban, D.; Sargent, E. H. Large piezoelectric response in a Jahn-Teller distorted molecular metal halide. *Nat. Commun.* **2023**, *14*, 1852.
(20) Halcrow, M. A. Jahn−Teller distortions in transition metal compounds, and their importance in functional molecular and inorganic materials. *Chem. Soc. Rev.* **2013**, *42*, 1784−1795.
(21) Sanz-Ortiz, M. N.; Rodriguez, F. Photoluminescence properties of Jahn-Teller transition-metal ions. *J. Chem. Phys.* **2009**, *131*, 124512.
(22) Chen, X.; Lu, W. G.; Tang, J.; Zhang, Y.; Wang, Y.; Scholes, G. D.; Zhong, H. Solution-processed inorganic perovskite crystals as achromatic quarter-wave plates. *Nat. Photonics* **2021**, *15*, 813−816.
(23) Kim, J.; Seo, O.; Tanaka, A.; Chen, J.; Watanabe, K.; Katsuya, Y.; Nabatame, T.; Irokawa, Y.; Koide, Y.; Sakata, O. Anisotropic mosaicity and lattice-plane twisting of an m-plane GaN homoepitaxial layer. *CrystEngComm* **2019**, *21*, 4036−4041.
(24) Wu, J.; Guzman, R.; Bao, S.; Zhang, Y.; Chen, Y.; Shen, S.; et al. Mosaic growth induced magnetic anisotropy in double perovskite $PrBaCo_2O_{5+\delta}$ thin films. *Acta Mater.* **2022**, *234*, No. 118040.
(25) Jin, J.; et al. Octahedral Distortion and Excitonic Behavior of $Cs_3Bi_2Br_9$ Halide Perovskite at Low Temperature. *J. Phys. Chem. C* **2023**, *127*, 3523−3531.
(26) Choi, Y.; Koo, D.; Jeong, G.; Kim, U.; Kim, H.; Huang, F.; Park, H. A vertically oriented two-dimensional Ruddlesden−Popper phase perovskite passivation layer for efficient and stable inverted perovskite solar cells. *Energy Environ. Sci.* **2022**, *15*, 3369−3378.
(27) Patel, S. N.; Glaudell, A. M.; Peterson, K. A.; Thomas, E. M.; O'Hara, K. A.; Lim, E.; Chabinyc, M. L. Morphology controls the thermoelectric power factor of a doped semiconducting polymer. *Sci. Adv.* **2017**, *3*, No. e1700434.
(28) Saha, A.; Bhattacharya, K.; Chakraborty, A. K. Achromatic quarter-wave plate using crystalline quartz. *Appl. Opt.* **2012**, *51*, 1976−1980.
(29) *CrysAlisPro 1.171.39.45f*; Rigaku Oxford Diffraction, 2018.
(30) Dolomanov, O. V.; Bourhis, L. J.; Gildea, R. J.; Howard, J. A. K.; Puschmann, H. OLEX2: A Complete Structure Solution, Refinement and Analysis Program. *J. Appl. Crystallogr.* **2009**, *42*, 339−341.
(31) Sheldrick, G. M. SHELXT − Integrated Space-Group and Crystal-Structure Determination. *Acta Crystallogr. A* **2015**, *71*, 3−8.
(32) Sheldrick, G. M. Crystal Structure Refinement with SHELXL. *Acta Crystallogr. C* **2015**, *71*, 3−8.
(33) Lee, J.; Rovira, P. I.; An, I.; Collins, R. W. Rotating-compensator multichannel ellipsometry: Applications for real time Stokes vector spectroscopy of thin film growth. *Rev. Sci. Instrum.* **1998**, *69*, 1800−1810.
(34) Woollam, J. A.; et al. Overview of variable-angle spectroscopic ellipsometry (VASE): I. Basic theory and typical applications. *Optical Metrology: A Critical Review* **1999**, *10294*, 3−28.
(35) Fujiwara, H. *Spectroscopic Ellipsometry: Principles and Applications*; John Wiley & Sons, 2007.
(36) Tompkins, H.; Irene, E. A. *Handbook of Ellipsometry*; William Andrew, 2005.
(37) Jellison, G. E., Jr.; Modine, F. A. Parameterization of the optical functions of amorphous materials in the interband region. *Applied Physics Letters* **1996**, *69*, 371−373.
(38) Peiponen, K.-E.; Vartiainen, E. M. Kramers-Kronig relations in optical data inversion. *Physical Review B* **1991**, *44*, 8301.
(39) Uprety, P.; et al. Spectroscopic ellipsometry determination of optical and electrical properties of aluminum doped zinc oxide. *Applied Surface Science* **2017**, *421*, 852−858.
(40) Kresse, G.; Furthmüller, J. Efficiency of ab-initio total energy calculations for metals and semiconductors using a plane-wave basis set. *Comput. Mater. Sci.* **1996**, *6*, 15−50.
(41) Notario-Estévez, A.; Kozlov, S. M.; Viñes, F.; Illas, F. Electronic-structure-based chemical descriptors:(in) dependence on self-interaction and Hartree-Fock exchange. *Phys. Rev. B* **1996**, *54*, 11169−11186.
(42) Blöchl, P. E. Projector augmented-wave method. *Phys. Rev. B* **1994**, *50*, 17953−17979.
(43) Perdew, J. P.; Burke, K.; Ernzerhof, M. Generalized gradient approximation made simple. *Phys. Rev. Lett.* **1996**, *77*, 3865.
(44) Dudarev, S. L.; Botton, G. A.; Savrasov, S. Y.; Humphreys, C.; Sutton, A. P. Electron-energy-loss spectra and the structural stability of nickel oxide: An LSDA+U study. *Phys. Rev. B* **1998**, *57*, 1505.

https://doi.org/10.1021/jacs.3c05705
J. Am. Chem. Soc. 2023, 145, 18007−18014